Journal of Power Sources 659 (2025) 238443

Contents lists available at ScienceDirect

Journal of Power Sources

journal homepage: www.elsevier.com/locate/jpowsour

Early state of $Li_7La_3Zr_2O_{12}$/Li heterointerface in all-solid-state battery: causality dilemma between crack formation and Li-rich nanodendrites

Oana Cojocaru-Mirédin [a,b,*], Yucheng Zhou [c], André Weber [d], Alexandre Mussi [e], Dagmar Gerthsen [f], Bai-Xiang Xu [c]

[a] INATECH, University of Freiburg, Emmy-Noether-Straße 2, 79110, Freiburg im Breisgau, Germany
[b] I. Institute of Physics, RWTH Aachen University, Sommerfeldstraße 14, 52062, Aachen, Germany
[c] Mechanics of Functional Materials Division, Institute of Materials Science, Technische Universität Darmstadt, 64287, Darmstadt, Germany
[d] Institute for Applied Materials (IAM-ET), Karlsruhe Institute of Technology (KIT), Adenauerring 20b, 76131, Karlsruhe, Germany
[e] Univ. Lille, CNRS, INRAE, Centrale Lille, UMR 8207 - UMET – Unité Matériaux et Transformations, F-59000, Lille, France
[f] Laboratory for Electron Microscopy, Karlsruhe Institute of Technology (KIT), Engesserstr. 7, 76131, Karlsruhe, Germany

HIGHLIGHTS

- Presence of Li-nanodendrites in LLZO bulk close to the Li/LLZO heterointerface.
- Existence of a high density of dislocations in LLZO bulk proved by TEM.
- The strong Li segregation at the dislocations' cores leads to crack formation.
- No secondary phases are formed at the abrupt interface between Li and LLZO.

ABSTRACT

It has been argued that the $Li_7La_3Zr_2O_{12}$/Li hetero-interface in all-solid-state batteries is prone to decomposition and degradation during synthesis and cycling, leading to the formation of Li dendrites and their propagation inside the $Li_7La_3Zr_2O_{12}$ bulk. However, the exact formation mechanism of these dendrites, as well as their chemical composition, remains not fully understood until now due to the difficulty of quantifying the Li concentration within the battery materials.

Therefore, in this work, we employed atom probe tomography in conjunction with advanced transmission electron microscopy to investigate the $Li_7La_3Zr_2O_{12}$ bulk in the vicinity of the $Li_7La_3Zr_2O_{12}$/Li heterointerface, a region prone to crack formation and propagation. We discovered that numerous Li-nanodendrites are present inside the LLZO bulk close to the Li/LLZO interface and that these nanodendrites appear similar to cracks being filled by Li. Therefore, this study raises a possible dilemma of causality between the crack formation and Li segregation in LLZO grains.

Interestingly, advanced microscopy investigations prove the existence of a high density of dislocations within LLZO for some grains. Moreover, the finite element modeling suggests that the dislocations' cores can act as nucleation sites for strong Li segregation, leading to an increase in hydrostatic stress. This implies that this strong Li segregation at the dislocation cores and the resultant high hydrostatic stress might be the cause for the crack formation. Subsequently, Li can be further accumulated at the cracks, forming the Li-nanodendrites.

It is without doubt that the presence of such microscopic Li-rich nanodendrites in the as-deposited state will lead to the growth and propagation of the well-known macroscopic Li dendrites during cycling.

1. Introduction

$Li_7La_3Zr_2O_{12}$ (LLZO) solid electrolytes (SEs) with competitive ionic conductivities of above 10^{-4} S/cm are widely considered as promising promoters for the Li anode. Having Li as an anode is necessary to meet the requirements of electric vehicles due to its ultra-high specific capacity (theoretical value of 3860 mAh/g) and its lowest electrochemical potential (0 V, reference) [1]. LLZO SEs have long been considered a viable solution for suppressing the Li dendrite growth (observed for the liquid electrolytes) due to their high mechanical strength (shear modulus of ~100 GPa); in accordance with the model of Monroe and Newman (shear modulus of LLZO should be two-fold larger than that of Li, i.e. of ~4.8 GPa) [2]. However, it is now commonly accepted that Li dendrites form and propagate in the high-strength LLZO SE during cycling under limited current densities [3,4].

Two main mechanisms for Li transport at the LLZO SE/Li anode

* Corresponding author. INATECH, University of Freiburg, Emmy-Noether-Straße 2, 79110, Freiburg im Breisgau, Germany.
E-mail address: oana.cojocaru-miredin@inatech.uni-freiburg.de (O. Cojocaru-Mirédin).

https://doi.org/10.1016/j.jpowsour.2025.238443
Received 8 July 2025; Received in revised form 10 September 2025; Accepted 16 September 2025
Available online 27 September 2025

interface have been proposed. These mechanisms focus on Li dendrite formation and propagation through the LLZO polycrystalline SE. The first common Li transport mechanism is of a transgranular type, where Li propagates through the grains of LLZO between the Li anode (Li) and cathode. The second, more recent Li transport mechanism is of an intergranular type, where Li propagates mainly through the GBs of LLZO from one electrode to the other side [2,5]. Although these Li transport mechanisms are believed to take place during cycling, our very recent work has proved that Li strongly accumulates at the LLZO GBs, forming Li complexions already during the LLZO synthesis (not in contact with the Li anode and not yet cycled) [6], proving that Li transport in LLZO is much more complex and miscellaneous than expected.

Understanding the Li transport is essential for optimizing the performance of the solid-state batteries. Therefore, in the present work, we provide the true Li transport mechanism at the LLZO/Li interface, which exists during the synthesis of the Li|LLZO|Li cell. This is of crucial importance for a proper understanding of the Li transport mechanism during cycling. Specifically, these anomalous and confined Li dendrites formed during cell fabrication (synthesis of the LLZO pellet and/or coating of the Li anode) may represent sites for dendrite growth and propagation during cycling.

Atom probe tomography (APT) [7,8] in conjunction with (scanning) transmission electron microscopy (STEM) [9–13] have been employed to study the Li redistribution at the LLZO/Li heterointerface in 3D and down to the sub-nanometer level. Although LLZO is believed to be electrochemically and thermodynamically very stable when put in contact with metallic Li [14–16], we show that Li not only accumulates at the LLZO GBs, as proved recently [6], but also Li forms small dendrites within the LLZO bulk close to the LLZO/Li heterointerface. The composition of the LLZO/Li heterointerface, as well as of these small Li dendrites found within the LLZO bulk, is quantified, providing clear hints about possible exhaustive mechanisms taking place during cycling. Hence, this work opens new perspectives in terms of the quantification of Li transport at the LLZO/Li heterointerface in 3D and down to the sub-nanometer level, an important finding for battery applications.

2. Methodology

2.1. Cell preparation

In this work, cubic garnet-type structure electrolyte pellets, fabricated by Toshima Manufacturing Co. (synthesis process is kept

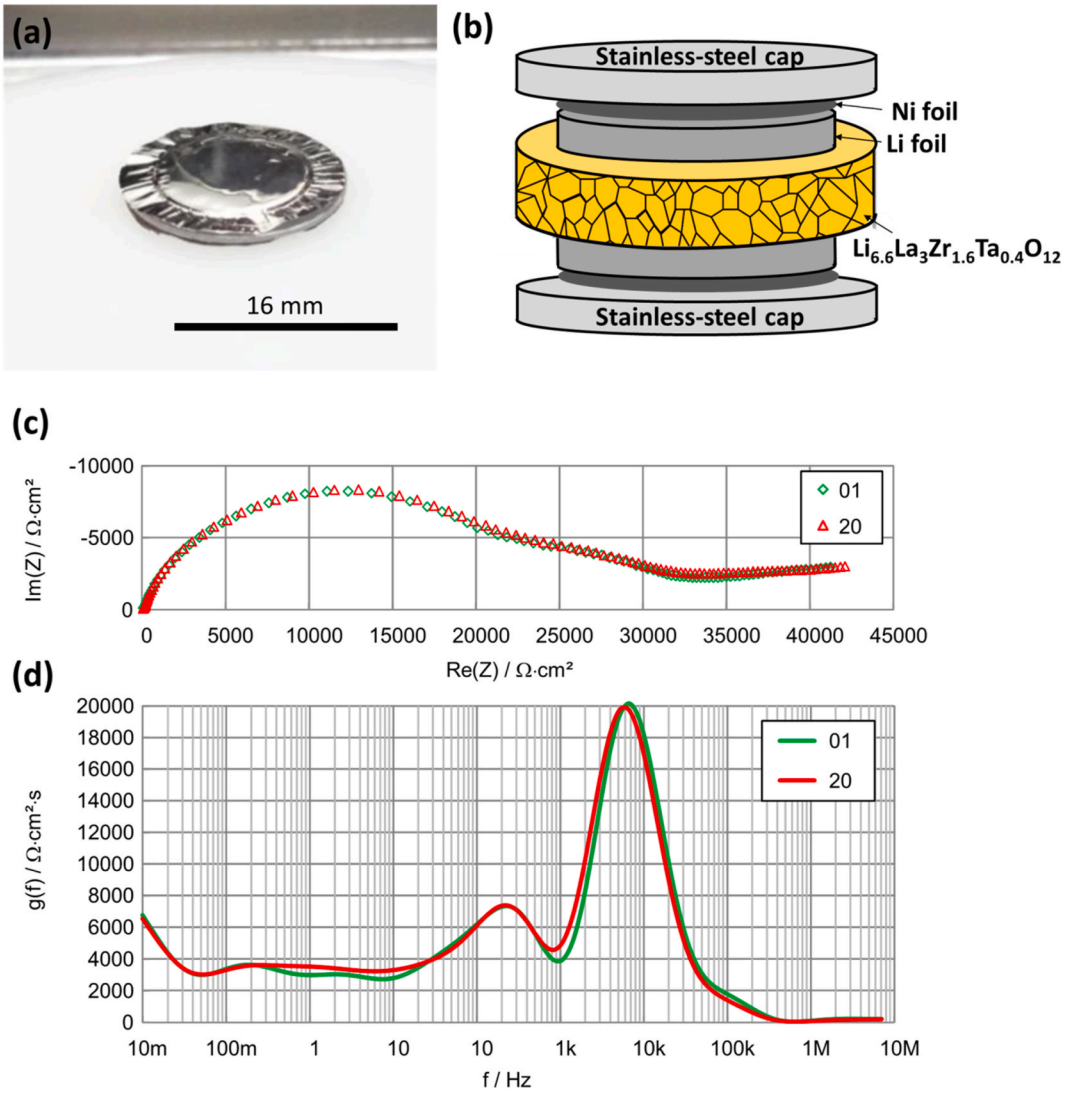

Fig. 1. Cell structure and EIS measurements of a symmetrical Li| LLZO| Li battery cell at *25°C. (a) A symmetrical model cell without the stainless-steel caps removed. The coining of the thin nickel foil provides additional stability. (b) Schematic structure of a symmetrical model cell according to the "sandwich principle". The individual components are stacked on top of each other by using a cell holder from bottom to top. c) EIS results. The Nyquist plot shows the spectra measured at the start (01) and, about 25 h later, the end (20) of a measurement series of 20 spectra. The related distribution of relaxation times (DRT) graphs are displayed in d).*

confidential), with a nominal chemical composition of $Li_{6.6}La_3Zr_{1.6}Ta_{0.4}O_{12}$, a pellet thickness d_p of about 500 μm, and a diameter of 16 mm are used for the battery cell fabrication (see Fig. 1b).

The steps used for cell fabrication (see Fig. 1a) are the same as the ones used in our recent work [17]. These individual steps were optimized to obtain reproducible symmetrical coin cells.

1. The LLZO pellets are polished with water-free diamond suspensions (*Struers* DP-Suspension A, 3 μm & 1 μm) to remove Li_2CO_3 and LiOH [18] and cleaned with 2-Propanol in between. It is well known that LiOH and Li_2CO_3 are formed if the LLZO SE surface is exposed to the air. The presence of these phases at the LLZO/Li interface results in poor wetting of the SE with the Li metal and, hence, a high resistance at the interface [17–19].
2. The cleaned LLZO pellet was transferred into an Ar-filled glovebox. Li electrodes of 1 cm^2 area and 500 μm thickness from Rockwood lithium foil were symmetrically attached to the LLZO surface.
3. Moreover, 10 μm nickel foils were attached to the top and bottom Li electrodes.
4. This battery cell was sandwiched between two stainless steel current collectors (1.6 mm thick).
5. Finally, a 220 °C heat treatment for 2h was performed in a vacuum oven (1 mbar). The temperature was chosen to be above the melting temperature of Li (180.5 °C) to improve the adhesion between the Li electrodes and LLZO SE.

After this procedure, the cell was mounted in an EL-cell housing (ECC-Std) for the impedance measurements. In this housing, the cell (16 mm in diameter, see Fig. 1a) is clamped by a spring applying a pressure of ~15 N, which corresponds to an insignificant pressure of only 0.075 MPa.

2.2. Electrochemical impedance spectroscopy and impedance data analysis

An electrical characterization by high-frequency impedance spectroscopy is performed with a *Biologic VMP 300* impedance analyzer in a frequency range from 7 MHz to 10 mHz. The perturbation voltage is set to 5 mV, and the impedance is averaged for every measured frequency over a total of 4 periods. The validity and residuals <1 % of the obtained impedance spectra are confirmed using the linear Kramers-Kronig Validity Test (Lin-KK Tool) [20].

As mentioned in section 2.1 above, optimized fabrication parameters for a direct Li/LLZO interface were employed. Subsequently, 20 spectra were measured, which all showed an excellent agreement, revealing that there is neither a rapid degradation nor noise affecting the impedance of the symmetrical cell. Fig. 1c shows 2 electrochemical impedance spectra measured at the start and end, respectively, and Fig. 1d the related distribution of relaxation times (DRT). The DRT-calculations considering the analyzed frequency range from 10 mHz to 7 MHz provide rather low series resistances of about 55 Ω cm^2 (not resolvable in the Nyquist plot) and high polarization resistances of 41.7 kΩ cm^2 and 42.5 kΩ $cm^{2,}$ respectively. The DRT reveals two main peaks at relaxation frequencies of ~200 and ~6000 Hz, respectively. These frequencies are much lower compared to the polarization attributed to the grains (at ~30 MHz) and the grain boundaries (at ~180 kHz) [17]. The observed increase in polarization resistances and decrease in the relaxation frequency f_R are in qualitative agreement with the fundamental relation $f_R = \sigma\cdot(2\pi\cdot\varepsilon_0\cdot\varepsilon_r)$, assuming that there are only minor changes in the materials' permittivity ε_r. A clear peak at ~1 Hz that was attributed to the interface in Ref. [17] cannot be resolved as further peaks in the low frequency region show a strong overlap. Yet, in our recent work [17], we have shown that by adding a 300 nm thick In layer at the LLZO/Li interface for the same cell structure described in section 2.1, the total resistance can be reduced by almost 200 times. If this reduction in total resistance is entirely due to the interface area, this will signify that only 0.5 % of the geometrical interface area is active (i.e. very poor adhesion of Li to LLZO), which is quite unlikely. Therefore, there is most probably also some increase in resistance due to the changes in chemistry at the interface. Another possibility to reduce this high contact resistance was mentioned by Janek et al. [21], where the Li|LLZO|Li structure was vacuum sealed in a plastic envelope, and an isostatic pressure of 400 MPa was applied to it. Yet, the goal of this study is to understand the chemical reactions happening at the LLZO/Li interface when Li and LLZO are put in direct contact. Application of any external parameters, such as isostatic pressure, will affect the Li diffusion characteristics at the interface level through the presence of deformation defects. Moreover, the experimental procedure applied above leads to multiple interfacial regions where the adhesion between Li and LLZO is very robust, as proven by the scanning electron microscopy (SEM) investigations in Fig. 2.

2.3. APT and (S)TEM experiments

The samples for the APT investigations are prepared accordingly to our previous work [6], as a needle-shaped specimen with a radius of the apex of about 30–40 nm, using the methodology described in Ref. [22] (GBs are placed perpendicular to the tip axis). Although no cryo-conditions were used during sample fabrication, very gentle parameters were applied during SEM imaging (5 keV, 100 pA) and focused ion beam (FIB) milling (final tip cleaning: 2 kV cleaning, 7 pA) so that Ga implantation and apex amorphization are strongly reduced. Very important is that the APT specimens are transferred immediately after sample fabrication to the APT analysis chamber and analyzed so that no Li out-diffusion during ultra-HV conditions takes place, as observed in our very recent studies (under publication) in agreement with ref. [23]. Moreover, the evaporation rate was maintained between $1\cdot10^{-2}$ and $0.5\cdot10^{-2}$ ions per pulse to preserve a high analysis yield for the Ta-doped LLZO material. Finally, the applied pulse repetition rate was not higher than 200 kHz to ensure the detection of all molecular ions on the mass spectrum, such as ZrO, ZrO_2, LaO, LaO_2, TaO, and TaO_2.

Similar very gentle final milling conditions (1 kV, 100 pA) were applied to prepare the TEM lamellae at the LLZO/Li interface with a thickness of about 50 nm. In this way, the crystallinity of the battery materials was preserved. Moreover, low current doses (few pA) at 60 kV and 200 kV were applied during the STEM investigations (using ADF: annular dark field condition in Fig. 3) to avoid any beam damage to the sample.

Dislocation analyses were carried out using the electron microscopy facility of the Advanced Characterization Platform of the Chevreul Institute, with a FEI® Tecnai $G^2$20Twin microscope, operating at 200 kV equipped with a LaB_6 filament. To reduce electron beam irradiation, characterizations were conducted in low dose conditions accordingly to previous work on sensitive minerals with electron beam [24]. TEM analyses were done with a spot size of 11.3 nm and a large diameter of the condenser aperture of 100 μm. Furthermore, pixels have been binned four by four to increase the signal-to-noise ratio of the weak-beam dark-field (WBDF) micrographs without increasing the electron dose.

3. Finite element modelling

3.1. Mechanically coupled diffusion model

The total free energy density of the system f combines chemical and elastic contributions,

$$f = f^c + f^e. \tag{1}$$

The chemical part f^c describes a regular solution,

$$f^c = RTc_{max}\,[c\ln c + (1-c)\ln(1-c) + \chi c(1-c)], \tag{2}$$

where R is the gas constant, T absolute temperature, c_{max} the maximum

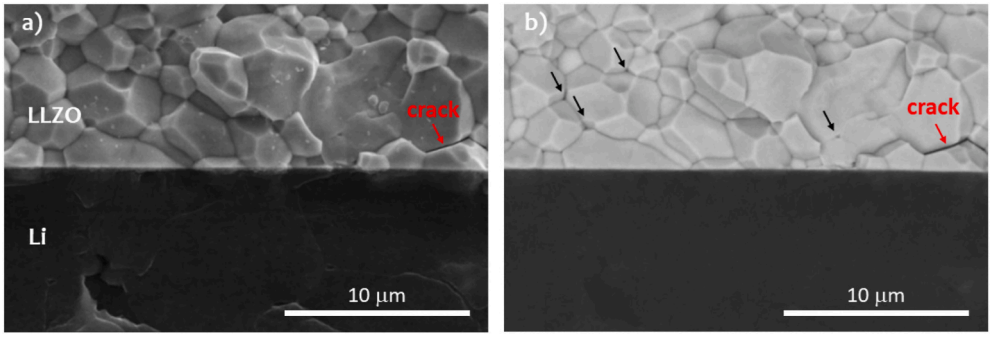

Fig. 2. Scanning electron microscopy (SEM) studies on freshly cleaved Li/LLZO/Li battery cells using 5 keV a) secondary electron–SEM image and b) backscattered-electron-SEM image. Grain boundaries (GBs) and triple junctions (see arrows) appear in dark contrast in b), which is a signature of the presence of low atomic-number phases, such as Li-based phases.

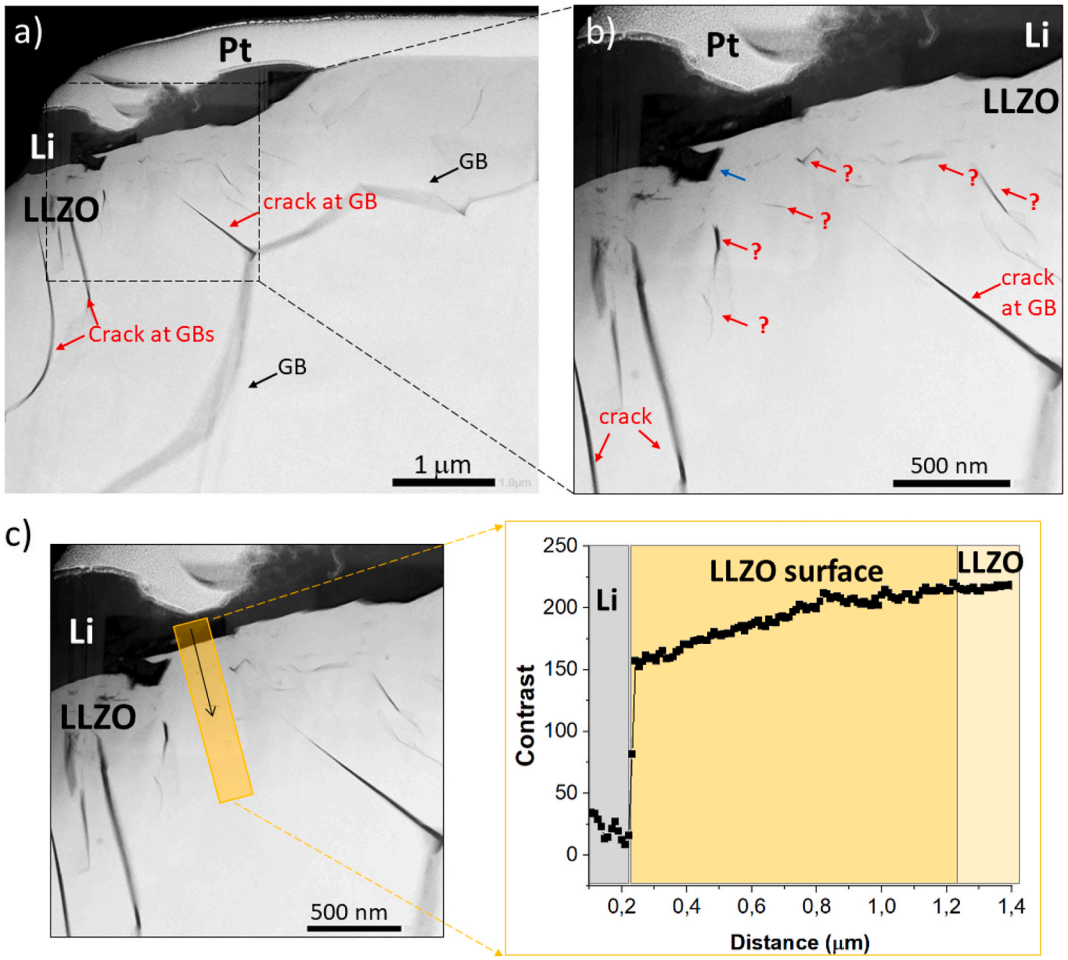

Fig. 3. ADF-STEM investigations of the LLZO/Li interface. a) Part of the TEM lamella is shown where the low-Z Li electrode ($Z^{1.7}$~6.5, where Z is the atomic number) is visible in black and the higher-Z LLZO SE (average $Z^{1.7}$~104) is visible in light-grey. Black arrows indicate the GBs decorated by Li, although cracks propagating along GBs are also highlighted in red. b) Blue arrow indicates a Li dendrite penetrating 200 nm deep inside the LLZO SE, and red arrows indicate most probably nanocracks filled by Li unexpectedly formed in the LLZO grain up to 3 µm deep from the LLZO/Li interface. c) The inset shows the contrast line profile across the LLZO/Li interface going deep down inside the LLZO. This profile may indicate a gradient in Li composition, more precisely, a decrease in Li composition with increasing distance from the LLZO/Li interface. (For interpretation of the references to colour in this figure legend, the reader is referred to the Web version of this article.)

solute concentration, c the normalized concentration by c_{max} ($0 \leq c \leq 1$), and χ the interaction parameter characterizing non-ideality. The elastic energy density f^e accounts for mechanical work,

$$f^e = \frac{1}{2}\sigma_{ij}\left(\varepsilon_{ij} - \varepsilon_{ij}^D - \varepsilon_{ij}^C\right). \quad (3)$$

The constitutive relationship connects stresses to elastic strains through Hooke's law for anisotropic materials,

$$\sigma_{ij} = C_{ijkl}\left(\varepsilon_{kl} - \varepsilon_{kl}^D - \varepsilon_{kl}^C\right). \quad (4)$$

Here, C_{ijkl} is the fourth-order elasticity tensor, ε_{kl} is the total strain, ε_{kl}^D

is the eigenstrain from dislocations, and ε_{kl}^{C} is the concentration-induced eigenstrain. The kinematic relationship between strains and displacements follows the small deformation assumption,

$$\varepsilon_{kl} = \frac{1}{2}\left(u_{k,l} + u_{l,k}\right), \tag{5}$$

where u_k represents displacement components. This symmetric gradient of the displacement field ensures compatibility of deformations. Dislocations create eigenstrains ε_{ij}^{D} that influence both stress and diffusion fields. For the straight edge dislocation considered in this work, we use a non-singular continuum formulation [25,26],

$$\varepsilon_{ij}^{D} = \frac{1}{2}\left(b_i n_j + b_j n_i\right) W(\mathbf{x}, h), \tag{6}$$

where b_i is the Burgers vector, n_j the slip plane normal, and $W(\mathbf{x}, h)$ a spreading function that regularizes the dislocation core over width h,

$$W(\mathbf{x}, h) = \int_S w(\| \mathbf{x} - \mathbf{x}^D \|, h)\, \mathrm{d}S. \tag{7}$$

This approach avoids singularities while maintaining accuracy outside core regions. The concentration-dependent eigenstrain caused by diffusive ions is expressed as

$$\varepsilon_{kl}^{C} = \frac{1}{3}\left(c - c_{\mathrm{ref}}\right)\Omega_{kl}, \tag{8}$$

where c is current ion concentration, c_{ref} reference concentration (stress-free state), and Ω_{kl} partial molar volume tensor of diffusive ions. This eigenstrain captures the lattice expansion/contraction resulting from ion insertion/extraction. When the local ion concentration c deviates from the reference concentration c_{ref}, the host material undergoes dimensional changes.

The mechanical equilibrium equation describes how stresses balance with body forces in the material domain B,

$$\sigma_{ij,j} + b_i = 0, \text{in } B, \tag{9}$$

where σ_{ij} represents the Cauchy stress tensor components and b_i are the body force components per unit volume. The comma notation indicates spatial derivatives (e.g., $\sigma_{ij,j} = \partial\sigma_{ij}/\partial x_j$). Boundary conditions complete the mechanical description,

$$u_i = \overline{u}_i, \text{on} \partial B_u. \tag{10}$$

$$\sigma_{ij} n_j = \overline{t}_i, \text{on} \partial B_\sigma. \tag{11}$$

These specify either prescribed displacements $\overline{u}_i$ on portion ∂B_u of the boundary or prescribed tractions $\overline{t}_i$ on ∂B_σ.

Mass conservation governs concentration evolution (Fick's second law),

$$\dot{c} + J_{i,i} = 0, \text{in } B. \tag{12}$$

The flux J_i follows from the gradient of chemical potential μ [27],

$$J_i = -M\mu_{,i}, \tag{13}$$

where M is the mobility coefficient. The chemical potential $\mu = \partial f / \partial c$ has both chemical and mechanical contributions [28],

$$\mu = \underbrace{RT\left[\chi(1-2c) + \ln\frac{c}{1-c}\right]}_{\text{Chemical part}} \underbrace{-\frac{1}{3}\sigma_{ij}\Omega_{ij}}_{\text{Stress coupling}}. \tag{14}$$

The mobility M depends on both solution thermodynamics and stress effects,

$$M = \frac{D_0 c_{\max}}{RT\left[\frac{1}{c(1-c)} - 2\chi\right] + \frac{1}{9}c_{\max} C_{ijkl}\Omega_{ij}\Omega_{kl}}. \tag{15}$$

where D_0 is the base diffusivity and Ω_{ij} the partial molar volume tensor.

The diffusion equation accounting for mechanical coupling contains third-order derivatives of the displacement field, which originate from stress gradient-induced drift effects. A conventional weak formulation based on concentration and displacement as the primary variables would require higher-order finite elements to properly resolve these derivatives. To address this challenge, a mixed finite element approach is adopted, wherein both concentration and chemical potential are treated as independent field variables. For a similar handling method, readers can also refer to Refs. [26,29]. This reformulation reduces the original third-order partial differential equation into two coupled second-order equations, which can be efficiently solved using standard linear finite elements.

3.2. Finite element formulation

The finite element formulation for Li-ion battery electrodes employs a coupled chemo-mechanical framework, where the Li-ion concentration field and mechanical displacement field are discretized using Galerkin's method. The weak forms of the Cahn-Hilliard-type diffusion equation (governing Li transport) and momentum balance (mechanical stress evolution) are solved simultaneously, with shape functions interpolating nodal values of concentration, chemical potential, and displacement. The nonlinear coupling arises from stress-dependent diffusion and concentration-dependent elasticity, necessitating Newton-Raphson iterations with consistent tangent matrices. In this work, the weak form formulations for finite element implementation are

$$\int_B \left(-\eta_{i,j}\sigma_{ij} + \eta_i b_i\right) \mathrm{d}V = 0, \tag{16}$$

$$\int_B \left(\eta\dot{c} - \eta_{,i} J_i\right) \mathrm{d}V = 0, \tag{17}$$

$$\int_B \eta\left[-\chi(1-2c) - \ln\left(\frac{c}{1-c}\right) + \frac{1}{3}\sigma_{ij}\Omega_{ij} + \mu\right] \mathrm{d}V = 0, \tag{18}$$

where η_i and $\eta_{i,j}$ are the test function and its gradient. The element-wise interpolations of η_i and $\eta_{i,j}$ based on shape functions are

$$\eta_i = \sum_I N^I \eta_i^I, \eta_{i,j} = \sum_I N_{,j}^I \eta_i^I, \tag{19}$$

where N^I is the shape function and η_i^I are the corresponding nodal values. The superscript I is the node number. The elemental residuals are

$$R_{u_i}^I = \int_{B^e} \left(-N_{u,j}^I \sigma_{ij} + N^I N_u^I b_i\right) \mathrm{d}V, \tag{20}$$

$$R_c^I = \int_{B^e} \left(N_c^I \dot{c} - N_{c,i}^I J_i\right) \mathrm{d}V, \tag{21}$$

$$R_\mu^I = \int_{B^e} N_\mu^I \left[-\chi(1-2c) - \ln\left(\frac{c}{1-c}\right) + \frac{1}{3}\sigma_{ij}\Omega_{ij} + \mu\right] \mathrm{d}V, \tag{22}$$

where N_u^I, N_c^I, and N_μ^I are the shape functions for u_i, c, and μ, respectively.

The mixed finite element formulation adopts independent nodal degrees of freedom for the displacement u_i, concentration c, and chemical potential μ. This approach is implemented using the MOOSE framework. All field variables are discretized using conventional linear Lagrange elements, ensuring C^0 continuity throughout the computational domain. To maintain numerical consistency, the function $W(\mathbf{x}, h)$ is treated as element-wise constant. This approximation ensures that the dislocation-induced eigenstrain is integrated with the same numerical order as the total strain. Such treatment effectively mitigates plastic incompatibility at element boundaries and prevents the emergence of

artificial stress concentrations, commonly referred to as "spurious stresses" [26].

4. Results and discussions

SEM was used to visualize the structural and chemical roughness at the LLZO/Li interface. The topography of the cleaved LLZO/Li interface is shown in the secondary-electron SEM image in Fig. 2a. The existence of different phases can be visualized by backscattered-electron SEM imaging in Fig. 2b, where the number of backscattered electrons reaching the backscattered-electron detector increases with the average atomic number of the imaged material. The backscattered-electron-SEM intensity can be either very low (Z = 3 for pure Li) or much higher (average atomic number Z = 18.4 for LLZO, neglecting Ta doping). Interestingly, besides the Li electrode, triple junctions and GBs of LLZO appear as dark-contrast regions in agreement with our recent work [6].

Although the LLZO/Li interface seems to be very clean and abrupt in Fig. 2b (the same observed for other larger regions, but not shown here), there are regions where Li and LLZO are intermixed, leaving doubts about the claimed stability of the LLZO/Li interface [14–16]. These regions are highlighted in and are systematically found along the LLZO/Li interface. We note here that to better visualize these regions, the sample was polished using a diamond paper with very small grain sizes (~50 nm) within a water-free solution and finally cleaned with 2-Propanol as described in the Methodology section.

Interestingly, cracks form and propagate along some GBs (see red arrow in Fig. 2), especially in the vicinity of the LLZO/Li interface, opening the question of the role of the stress field that arises already during the as-deposited state (before cycling). Formation of such cracks in battery materials has already been confirmed for polycrystalline NMC (nickel–manganese–cobalt) cathode active materials during the first cycles, allowing the solid electrolyte to penetrate within the active material [30].

ADF-STEM investigations were done to better visualize possible chemical intermixing between Li and LLZO. In ADF, we have a superposition of two contrasts, diffraction contrast and Z contrast, which makes it difficult to directly relate the contrast changes to the composition. Yet, the Li metal appears black in Fig. 3, similarly with the one expected in the high angular annular dark-field (HAADF) mode for Li [31] (in the HAADF-STEM intensity proportional to $Z^{1.7}$, given that Z for Li is only ~6.5, where Z is the atomic number). Moreover, some of the GBs appear in Fig. 3a in dark contrast, suggesting that these GBs are decorated by elements with rather low atomic mass, namely Li. This was demonstrated by our recent work, where a high quantity of Li was found accumulated at the GBs in LLZO (up to almost 90 at.%) [6]. Interestingly, cracks are also visible along some GBs (highlighted by red arrows), which agrees with the SEM observations from Fig. 2.

A Li dendrite growing from the Li electrode inside the LLZO is highlighted by a blue arrow in Fig. 3b. Yet, this Li dendrite does not seem to penetrate along the GBs of LLZO as claimed by many recent works [2,32,33], but rather inside the LLZO bulk (or grain). One has to mention here that the heat treatment at 220 °C employed here exceeds the Li melting temperature of ~180.5 °C, which suggests that empty holes found at the LLZO surface might get filled by liquid Li, thus improving the surface coverage.

Last but not least, interestingly small curved features (see red arrows in Fig. 3b) with very different lengths (but below 500 nm) and shapes are found in LLZO, within the first 3 μm from the LLZO/Li heterointerface. They appear as filled nanocracks. Their presence in the LLZO bulk was until now unknown in the literature. Hence, these ADF-STEM investigations open new questions regarding their origin and composition.

Interestingly, in Fig. 3c, one can see a gradient in contrast when going from the LLZO/Li interface inside the LLZO bulk of about 1–2 μm deep. Although a direct quantitative comparison cannot be made (ADF mode and not HAADF), this result can nevertheless indicate qualitatively a gradient in Li composition, i.e., Li composition decreases with increasing distance from the LLZO/Li interface.

By leveraging the power of the APT, we are now able to unveil the previously hidden composition of the LLZO/Li heterointerface that was not observable before using the conventional methods (difficulty in quantifying Li). Fig. 4 summarizes the APT results obtained on the LLZO/Li heterointerface. A rather high O content was unexpectedly detected inside the Li anode material, close to the LLZO/Li interface. At first glance, one may argue that Li is oxidized during the short sample transfer and pumping (a few minutes) of the APT specimen. It is known indeed that Li reacts in the air to produce Li_2O ($4Li + O_2 \rightarrow 2LiO_2$) and Li_3N ($6Li + N_2 \rightarrow 2Li_3N$). Yet, no N was detected inside Li (air contains both N (78 %) and O (21 %)). Besides O, Zr is detected inside the Li anode too (most probably in the form of ZrO_2 in the vicinity of the LLZO/Li interface), suggesting that Zr and O are originating from the LLZO: O and Zr diffusion from LLZO inside Li during Li|LLZO|Li cell fabrication. The potential release of O from the garnet LLZO is not new and has already been proven to be responsible for thermal runaway in the cell [34].

Even if the Zr and O had diffused inside the Li anode during synthesis, a quite abrupt interface (a few nm wide only) is still clearly visible in Fig. 4c. This is not contradicting the results shown in Fig. 3c, given that here a very narrow region around the interface was measured (of about 100 nm), well below the gradient observed over the 1–2 μm in Fig. 3c. No secondary phases are present at this hetero-interface in any of the analyses performed. This suggests that the Li transport between the anode and the solid electrolyte remains very efficient and that minimal diffusion barriers or interfacial resistance might be present. Hence, these APT and STEM results suggest that the interface between Li and LLZO is rather chemically abrupt and structurally stable. Yet, interestingly, both mixed Li-LLZO regions (Fig. 5a), as well as small chemical instabilities that assemble to filled nanocracks (Fig. 5b), have been observed in the close vicinity of the LLZO/Li heterointerface (see Fig. 3b), for which their origin and composition are still unknown.

Therefore, these nanocracks have been characterized with APT, and the results obtained are summarized in Fig. 5. Two Li-rich nanocracks are identified in Fig. 5c, given that these Li-rich nanocracks were extracted from the LLZO bulk region, in the vicinity of the LLZO-Li heterointerface. It is important to mention here that such Li-nanodendrites were not present in the LLZO bulk far away from the interface region [6]. Interestingly, the Li and O compositions of these Li-nanocracks seem to vary strongly (60–70 at.% for Li and 20 to 30 at.% for O, see Table 1), which recalls the composition of the GBs in LLZO [6]. Thus, these nanocracks present in the vicinity of the LLZO/Li heterointerface trap Li and, therefore, they can be considered as artificial Li-nanodendrites. Hence, this work opens a possible dilemma of causality between the crack formation and Li-segregation; i.e. the presence of the nanocracks leads to Li strong segregation to fill these cracks, or the strong Li accumulation at specific structural defects leads to crack formation and propagation.

The composition of the LLZO bulk found in the vicinity of the LLZO/Li interface is very stable (see Table 1), but the average Li composition of 29.75 at.% (see Table 1) is way superior to the one measured inside the LLZO bulk (20.9 at.% Li) in our previous work [6]. Moreover, this average Li composition of 29.75 at.% is very close to the expected nominal composition of 29.1 at.% Li in LLZO solid electrolyte. The only difference between this and previous work [6] is that the LLZO solid electrolyte in this work is directly sandwiched in-between two thin Li layers, proving the importance of encapsulating the LLZO solid electrolyte to avoid any loss in Li (due to the secondary phase formation, such as Li_2CO_3 and LiOH, in contact with the air). This higher Li content in the near vicinity of the LLZO/Li interface is consolidated by the results in Fig. 3c, where clearly a contrast gradient, i.e. a Li gradient, is observed within the first 1–2 μm.

The insufficient contact and the presence of voids at the interface lead to poor wetting between the Li anode and the LLZO solid electrolyte. This is the main reason for the increased resistance measured here

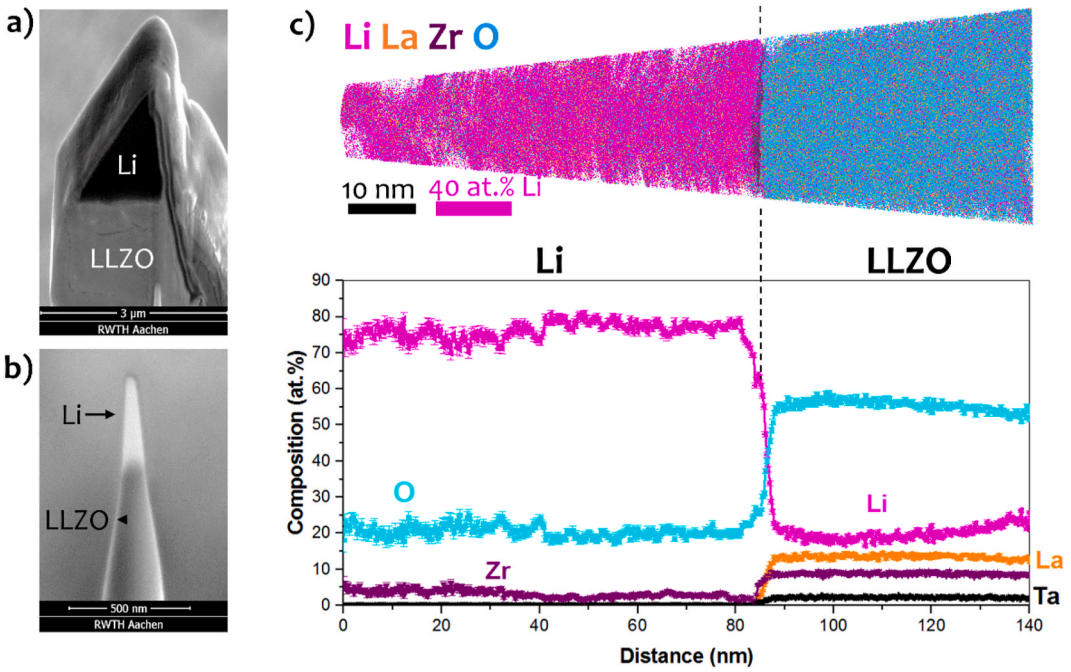

Fig. 4. APT investigations of the LLZO/Li heterointerface. a,b) Chunk and APT needle containing the LLZO/Li heterointerface. The interface is placed within the first 500 nm from the apex of the final APT needle. c) Three-dimensional APT map showing the distribution of Li (pink), La (orange), Zr (violet), O (light-blue), and Ta (black) atoms. The position of the LLZO/Li heterointerface is highlighted by a dotted line. Below, the 1D composition profile of all elements identified is given, highlighting the two regions: Li anode and LLZO solid electrolyte. (For interpretation of the references to colour in this figure legend, the reader is referred to the Web version of this article.)

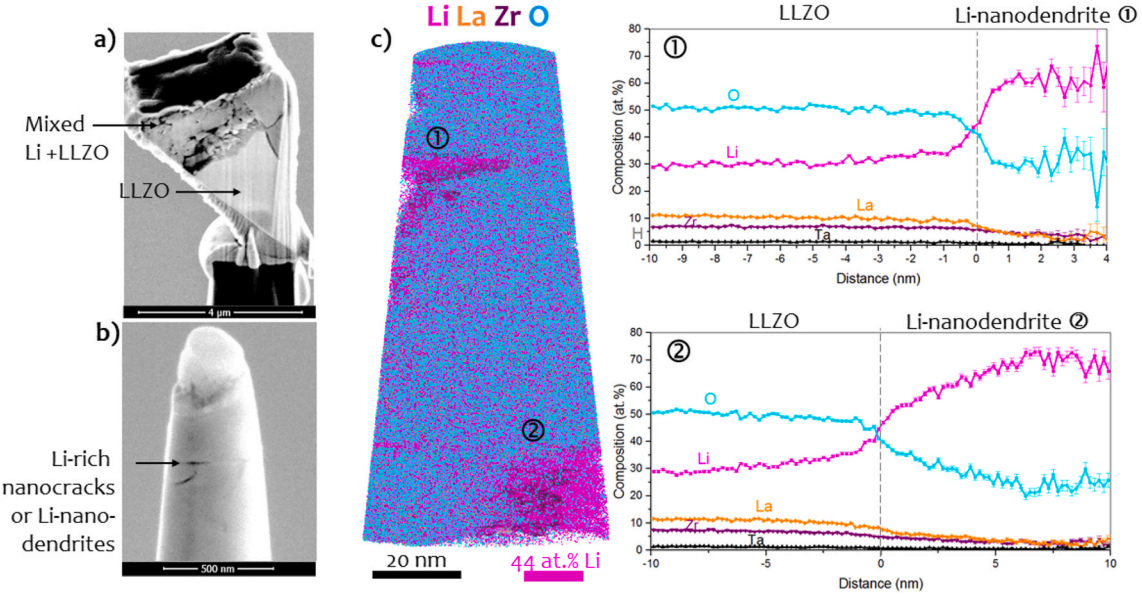

Fig. 5. APT investigations of the Li-rich nanocracks or artificial Li-rich nanodendrites. a,b) Part of the lamellae and APT needle containing both the mixed Li-LLZO regions and the Li-rich dendrites. c) Three-dimensional APT map showing the distribution of Li (pink), La (orange), Zr (violet), O (light-blue), and Ta (black) atoms. Two Li-rich dendrites could be identified. The proximity histogram of each respective dendrite is given. The proximity histograms have been constructed using the Li iso-surface of 42 at.%. The "0" position marks the interface between the LLZO bulk (left) and the Li-nanodendrite (right). (For interpretation of the references to colour in this figure legend, the reader is referred to the Web version of this article.)

with EIS. We have indeed recently proved that the addition of a 300 nm thick In layer at the interface between the Li anode and LLZO SE drastically reduces the interface resistance [17]. Moreover, these voids present at the interface allow for the Li-dendrites to grow, as marked by the blue arrow in Fig. 3. Interestingly, besides these well-known Li-dendrites formed at the LLZO/Li interface, the presence of Li-nanodendrites in the LLZO bulk, close to the LLZO/Li interface, has never been mentioned before. We seek now to comprehend why these Li-nanodendrites or Li-rich nanocracks are formed in the LLZO bulk, in the vicinity of the LLZO/Li Interface.

Although LLZO possesses high mechanical strength (high shear modulus of ~100 GPa) [2], the weak mechanical properties of the LLZO/Li interface might represent the reason for the formation of such small Li-nanocracks or nanodendrites inside the LLZO bulk at a distance

Table 1
The atomic composition of the LLZO bulk and Li-nanodendrites (Li-NDs) obtained by the APT investigations. Although the elemental composition in LLZO bulk is rather constant, the Li and O composition varies strongly within the Li-nanodendrites.

Region	Li (at.%)	La (at.%)	Zr (at.%)	Ta (at.%)	O (at.%)
Bulk ①	29.4 ± 0.3	11.3 ± 0.2	7.15 ± 0.2	1.34 ± 0.1	50.6 ± 0.3
Li-ND ①	**69.2 ± 1.5**	2.7 ± 0.2	2.7 ± 0.2	0.5 ± 0.1	**23.8 ± 1.2**
Bulk ②	30.1 ± 0.4	10.6 ± 0.2	6.9 ± 0.2	1.35 ± 0.1	50.8 ± 0.4
Li-ND ②	**60.7 ± 1.5**	3.5 ± 0.5	4.1 ± 0.5	0.56 ± 0.07	**30.7 ± 1**

of up to 3 μm from the interface region. The lattice mismatch (LM) between the Li film and LLZO is very high at about 270 %, given that the lattice mismatch is defined as LM $= \frac{(a-b)}{b} \times 100$, where a is the lattice parameter for LLZO(100) of 12.98 Å, whereas b is the lattice parameter of Li(100) of 3,51 Å. The accommodation of such high hydrostatic stress (σ_h) or volumetric stress can be realized either by strong interdiffusion between Li and LLZO at the hetero-interface region or by the formation of misfit dislocations.

In the following, the chemo-mechanical model introduced by Zhou et al. [35] is implemented into the finite element method (FEM) to derive the Eshelby stress tensor derived from the gradient of the total free energy density f for the mechanical coupled diffusion problem. Fig. 6a) shows that in the absence of misfit dislocations at the LLZO/Li heterointerface, a strong and gradient-like interdiffusion is expected between Li and LLZO. Yet, this is contrary to the observations done by APT: the LLZO/Li heterointerface was chemically rather abrupt. Interestingly, when misfit dislocations were considered at the LLZO/Li heterointerface (Fig. 6b), the interdiffusion between LLZO and Li is reduced, in agreement with the APT results. Yet, regarding applicability, the presence of misfit dislocations at the LLZO/Li heterointerface can cause irreversible degradation of the electrochemical performance due to the reduced interface mobility. This might be one of the main reasons for fatigue crack formation and the presence of such mixed LLZO-Li regions at the LLZO/Li heterointerface (as highlighted in Fig. 5a).

Interestingly, the presence of misfit dislocations at the LLZO/Li heterointerface in Fig. 6b (a scenario which describes the best the APT results as described above) leads to the formation of a hydrostatic stress (σ_h) with the two components, i.e. compressive (in blue) and tensile (in red) stress fields localized at the LLZO/Li heterointerface. In this case, very little stress is propagated towards the LLZO bulk. We note here that the tensile stress tends to increase the Li local concentration, whereas the compressive stress suppresses it (see Fig. 6).

We note here that in our simulation, we applied Neumann zero-flux boundary conditions on the left and right edges of the domain (Fig. 6a) to better reflect realistic experimental settings. These conditions constrain the Li flux across the boundaries ($\partial c/\partial x = 0$), preventing artificial exchange with the surroundings. However, they do not enforce uniform concentration along the x-direction. As the system evolves from the initial concentration step, it minimizes its total chemo-mechanical energy. The constrained flux leads to a slight lateral concentration

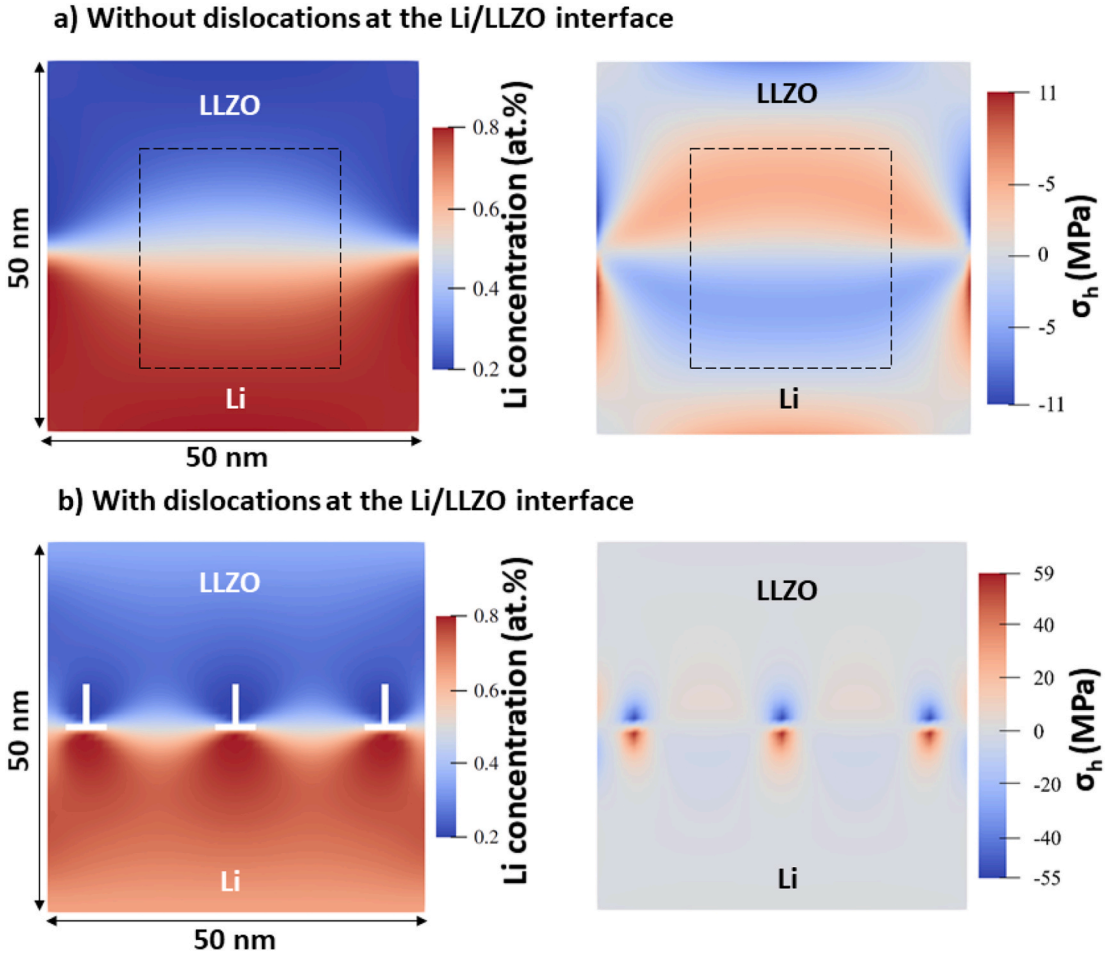

Fig. 6. Representation of the chemo-mechanical model at the LLZO/Li heterointerface using the finite element method. Equilibrium concentration without (a) and with misfit dislocations (b) present at the LLZO/Li heterointerface. Distribution of the hydrostatic stress (σ_h) for both cases, i.e., without and with misfit dislocations. The tensile stress fields (in red) are in the high Li concentration regions, while the compressive stress fields (in blue) are in the low concentration regions. (For interpretation of the references to colour in this figure legend, the reader is referred to the Web version of this article.)

gradient, especially near the interface. This, in turn, influences the hydrostatic stress distribution, which is strongly coupled to local Li concentration via both chemical expansion and reference concentration mismatches. High-Li regions develop tensile stress, while low-Li regions exhibit compressive stress, resulting in asymmetric stress profiles that mirror the concentration field. For analysis, we focus on the central region of the domain (highlighted by a dashed rectangle), where boundary effects are minimal and the intrinsic chemo-mechanical behavior is accurately captured. This ensures both physical relevance and numerical reliability.

The presence of misfit dislocations at the LLZO/Li heterointerface does not explain the presence of nanocracks or Li-nanodendrites in the LLZO bulk, in the vicinity of the heterointerface. Therefore, advanced TEM analyses under WBDF conditions were performed to determine if dislocations are present in LLZO SE close to the Li anode. A very high density of dislocations could indeed be observed (see Fig. 7a), which complicated the determination of the exact dislocation density. Moreover, some grain contains a very high dislocation density (pile-up and dislocation interaction effects), while others seem to contain less (see Fig. 7b–g). Burgers vectors (**b**) in garnet are generally ⟨100⟩ and $\frac{1}{2}\langle 111\rangle$ [36,37], more specifically, in the FIB specimen of this study, dislocations are seen by bringing the sample in the WBDF (g, ng) condition, with the reciprocal lattice vector g and $n > 1$ [38]. A dislocation, in white in Fig. 7e–f (in contrast), may have a [010] *or* a $\frac{1}{2}\langle 111\rangle$ Burgers vector and another dislocation, in black in Fig. 7e–f ($\mathbf{g}.\mathbf{b} = 0$ with a black residual contrast), may have a [100] or a [001] Burgers vector. The existence of a high local dislocation density ρ is a signature of a high local stress. Indeed, the internal stress increases according to the Taylor Law ($\Delta\tau = \alpha\mu b\sqrt{\rho}$), where α is a constant factor of 0.35 ± 0.15 which depends on the dislocation junction type [39], μ is the shear modulus, ρ is the dislocation density, and b is the Burger vector. Hence, a strong plastic deformation takes place within LLZO. Yet, this SE was originally doped with Ta to consolidate its cubic structure during Li flow (i.e. during volumetric changes) [40]. More exactly, the Ta doping generates a solid solution hardening by the Cottrell atmosphere effect $\Delta\tau = \beta c^{2/3}$ with β a constant and c the concentration of Ta [41].

Thanks to the TEM studies, it becomes clear that a high density of dislocations is present in the LLZO bulk, in the vicinity of the LLZO/Li heterointerface. Yet, the question is whether these dislocations are the reason for the formation of Li-rich nanodendrites as observed by APT. To answer this question, we calculated here the Li concentration around edge dislocations in LLZO using FEM (Fig. 8, left). From these FEM simulations, it becomes clear that Li is inhomogenously redistributed around a dislocation.

Moreover, dislocations are not ideally straight in real materials and can indeed contain both screw and edge components. The elastic fields are then described as a superposition of the stress fields of the screw and edge dislocation. Given that only the edge component causes a hydrostatic stress, the defects can only interact with the edge component. Therefore, in this work, we will focus on edge dislocations only. The results obtained can be extrapolated to curved dislocations, where the strongest interaction will be in areas with pure edge component and will decrease with increasing screw component.

From Fig. 8, it becomes clear that Li tends to accumulate at the edge side of the dislocation, which is found under tensile stress fields (in red), whereas Li is depleted at the dislocation line found under compressive stress fields (in blue). This is especially true for Li^+, which is the ion with the lowest ionic radius and mass (except for Hydrogen and Helium) and,

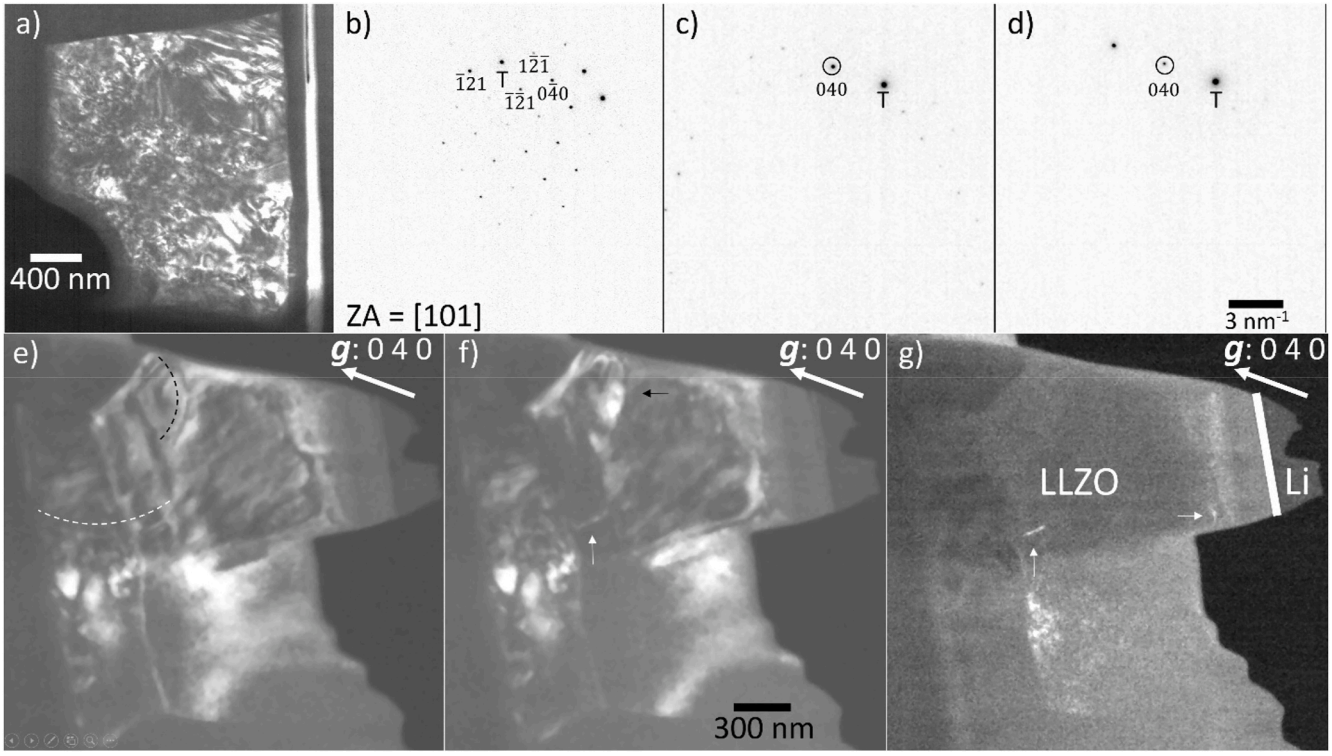

Fig. 7. Dislocation microstructure of the LLZO/Li interface. a) High dislocation density domain located in LLZO (in the lower part of the FIB specimen). b) Diffraction pattern along the [101] zone axis, in LLZO (in the upper part of the FIB specimen). c,d) Diffraction pattern with a small deviation from b), in Bragg condition (g = 040) and weak-beam dark-field $(g, 2g)$ condition. e) Conventional dark-field micrograph corresponding to c), a dislocation pointed out by a white dashed circular arc is in contrast (maybe a dislocation with a [010] Burgers vector), while a dislocation pointed out by a black dashed circular arc is out of contrast (may be a dislocation with a [100] or a [001] Burgers vector). f) Weak-beam dark-field micrograph corresponding to d), the dislocation in contrast is pointed out by a small white arrow, and the dislocation out of contrast is pointed out by a small black arrow. g) Weak-beam dark-field micrograph in (g, ng) condition with $n > 2$, the dislocations in contrast are seen (it is worth noticing another dislocation with this illumination condition), the interface between Li and LLZO is indicated with a thick white line.

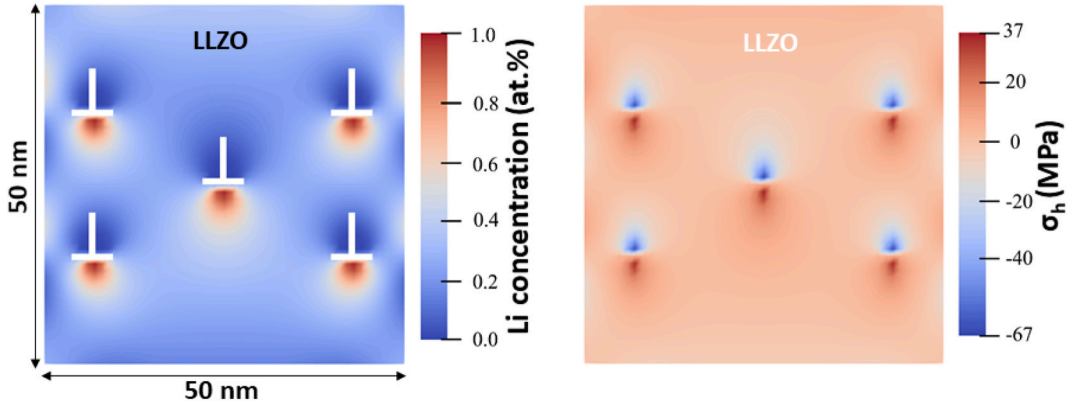

Fig. 8. Representation of the edge dislocations using the finite element method. Left: Li concentration inside the LLZO bulk and around the edge dislocations. Right: Distribution of the hydrostatic stress (σ_h) inside the LLZO bulk and around the edge dislocations showing the compressive (in blue) and tensile (in red) stress fields. (For interpretation of the references to colour in this figure legend, the reader is referred to the Web version of this article.)

hence, highly mobile within LLZO. We note here that the Li segregation will slow down the movement of dislocations by a "solute drag effect", which will tend to increase the density of dislocations and thus increase internal stresses in tension as well as in compression. Where internal stresses in tension are greatest, micro-cracks will appear.

This implies that this strong Li segregation at the dislocation cores and the resultant high tensile stress might be the cause for the crack formation. Subsequently, the Li can further fill the cracks formed to ultimately obtain the Li-nanodendrites observed by APT. This is in agreement with the work of Li et al. [42] who had demonstrated that tensile stress in solid-state batteries induces crack formation and propagation. Such a tensile stress field exists either due to the presence of structural defects (such as dislocations) enriched in Li or due to Li-extraction or insertion during battery cycling. Hence, this work proves an intimate relationship between dislocations, Li segregation, and crack formation in the LLZO solid electrolyte.

5. Conclusions

The present work proves the presence of Li-nanodendrites inside the LLZO bulk close to the Li/LLZO heterointerface. Advanced TEM investigations prove the existence of a high density of dislocations within LLZO. These TEM results, corroborated with the APT results, suggest that the strong Li segregation at the dislocations' cores leads to crack formation, i.e. Li-nanodendrites formation by filling of the empty cracks with Li freely available. Moreover, the interface between Li and LLZO is stable and abrupt, with no presence of other secondary phases.

CRediT authorship contribution statement

Oana Cojocaru-Mirédin: Writing – original draft, Validation, Supervision, Resources, Project administration, Methodology, Funding acquisition, Conceptualization. **Yucheng Zhou:** Methodology, Investigation, Data curation. **André Weber:** Supervision, Software, Investigation, Data curation, Conceptualization. **Alexandre Mussi:** Writing – original draft, Formal analysis, Data curation. **Dagmar Gerthsen:** Writing – original draft, Project administration, Methodology, Conceptualization. **Bai-Xiang Xu:** Supervision, Data curation, Conceptualization.

Declaration of competing interest

The authors declare that they have no known competing financial interests or personal relationships that could have appeared to influence the work reported in this paper.

Acknowledgments

The Chevreul Institute is thanked for its help in the development of this work through the ARCHI-CM project supported by the "Ministère de l'Enseignement Supérieur de la Recherche et de l'Innovation", the region "Hauts-de-France", the ERDF program of the European Union and the "Métropole Européenne de Lille". The electron microscopy facility of the Chevreul Institute is also supported by the INSU. OCM and AM thank the European Campus EUCOR for providing the funds (QuBAT Project) necessary for conducting the advanced TEM investigations.

Data availability

Data will be made available on request.

References

[1] X.-B. Cheng, R. Zhang, C.-Z. Zhao, Q. Zhang, Toward safe lithium metal anode in rechargeable batteries: a review, Chem. Rev. 117 (15) (Aug. 2017) 10403–10473, https://doi.org/10.1021/acs.chemrev.7b00115.
[2] D. Cao, X. Sun, Q. Li, A. Natan, P. Xiang, H. Zhu, Lithium dendrite in all-solid-state batteries: growth mechanisms, suppression strategies, and characterizations, Matter 3 (1) (2020) 57–94, https://doi.org/10.1016/j.matt.2020.03.015.
[3] H. Gao, et al., Visualizing the failure of solid electrolyte under GPa-level interface stress induced by lithium eruption, Nat. Commun. 13 (1) (2022) 5050, https://doi.org/10.1038/s41467-022-32732-z.
[4] F. Han, et al., High electronic conductivity as the origin of lithium dendrite formation within solid electrolytes, Nat. Energy 4 (2019) 187–196.
[5] E.J. Cheng, A. Sharafi, J. Sakamoto, Intergranular Li metal propagation through polycrystalline Li6.25Al0.25La3Zr2O12 ceramic electrolyte, Electrochim. Acta 223 (2017) 85–91, https://doi.org/10.1016/j.electacta.2016.12.018.
[6] O. Cojocaru-Mirédin, J. Schmieg, M. Müller, A. Weber, E. Ivers-Tiffée, D. Gerthsen, Quantifying lithium enrichment at grain boundaries in Li7La3Zr2O12 solid electrolyte by correlative microscopy, J. Power Sources 539 (January) (2022), https://doi.org/10.1016/j.jpowsour.2022.231417.
[7] B. Gault, et al., Atom probe tomography, Nat. Rev. Methods Prim. 1 (1) (2021), https://doi.org/10.1038/s43586-021-00047-w.
[8] D. Blavette, et al., Laser-assisted atom probe tomography and nanosciences 99 (5) (2008) 454–460, https://doi.org/10.3139/146.101672.
[9] O. Cojocaru-Mirédin, A. Devaraj, Correlative microscopy and techniques with atom probe tomography: opportunities in materials science, MRS Bull. 47 (7) (2022) 680–687, https://doi.org/10.1557/s43577-022-00369-4.
[10] O. Cojocaru-Mirédin, T. Schwarz, D. Abou-Ras, Assessment of elemental distributions at line and planar defects in Cu(In,Ga)Se2 thin films by atom probe tomography, Scr. Mater. 148 (2018) 106–114, https://doi.org/10.1016/j.scriptamat.2017.03.034.
[11] A. Stoffers, et al., Correlating atom probe tomography with atomic-resolved scanning transmission electron microscopy: example of segregation at silicon grain boundaries, Microsc. Microanal. 23 (2) (2017) 291–299, https://doi.org/10.1017/S1431927617000034.
[12] C.H. Liebscher, et al., Strain-induced asymmetric line segregation at faceted Si grain boundaries, Phys. Rev. Lett. 121 (1) (2018) 1–5, https://doi.org/10.1103/PhysRevLett.121.015702.
[13] O. Cojocaru-Mirédin, H. Hollermann, A.M. Mio, A.Y.T. Wang, M. Wuttig, Role of grain boundaries in Ge-Sb-Te based chalcogenide superlattices, J. Phys. Condens. Matter 31 (20) (2019), https://doi.org/10.1088/1361-648X/ab078b.

[14] Y. Xiao, Y. Wang, S.H. Bo, J.C. Kim, L.J. Miara, G. Ceder, Understanding interface stability in solid-state batteries, Nat. Rev. Mater. 5 (2) (2020) 105–126, https://doi.org/10.1038/s41578-019-0157-5.
[15] M. Fingerle, C. Loho, T. Ferber, H. Hahn, R. Hausbrand, Evidence of the chemical stability of the garnet-type solid electrolyte Li5La3Ta2O12 towards lithium by a surface science approach, J. Power Sources 366 (2017) 72–79, https://doi.org/10.1016/j.jpowsour.2017.08.109.
[16] J. Wolfenstine, J.L. Allen, J. Read, J. Sakamoto, Chemical stability of cubic Li7La3Zr2O12 with molten lithium at elevated temperature, J. Mater. Sci. 48 (17) (2013) 5846–5851, https://doi.org/10.1007/s10853-013-7380-z.
[17] M. Müller, et al., Reducing impedance at a Li-metal anode/garnet-type electrolyte interface implementing chemically resolvable in layers, ACS Appl. Mater. Interfaces 14 (12) (Mar. 2022) 14739–14752, https://doi.org/10.1021/acsami.1c25257.
[18] A. Sharafi, et al., Impact of air exposure and surface chemistry on Li–Li7La3Zr2O12 interfacial resistance, J. Mater. Chem. A 5 (26) (2017) 13475–13487, https://doi.org/10.1039/C7TA03162A.
[19] Y. Li, et al., Garnet electrolyte with an ultralow interfacial resistance for Li-metal batteries, J. Am. Chem. Soc. 140 (20) (May 2018) 6448–6455, https://doi.org/10.1021/jacs.8b03106.
[20] M. Schönleber, D. Klotz, E. Ivers-Tiffée, A method for improving the robustness of linear kramers-kronig validity tests, Electrochim. Acta 131 (2014) 20–27.
[21] T. Krauskopf, H. Hartmann, W.G. Zeier, J. Janek, Toward a fundamental understanding of the lithium metal anode in solid-state batteries—an electrochemo-mechanical study on the garnet-type solid electrolyte Li6.25Al0.25La3Zr2O12, ACS Appl. Mater. Interfaces 11 (15) (Apr. 2019) 14463–14477, https://doi.org/10.1021/acsami.9b02537.
[22] O. Cojocaru-Mirédin, T. Schwarz, P.P. Choi, M. Herbig, R. Wuerz, D. Raabe, Atom probe tomography studies on the Cu(In,ga)Se2 grain boundaries, J. Vis. Exp. 74 (2013) 1–8, https://doi.org/10.3791/50376.
[23] S.-H. Kim, et al., Atom probe analysis of electrode materials for Li-ion batteries: challenges and ways forward, J. Mater. Chem. A 10 (9) (2022) 4926–4935, https://doi.org/10.1039/D1TA10050E.
[24] A. Mussi, J. Gallet, O. Castelnau, P. Cordier, Application of electron tomography of dislocations in beam-sensitive quartz to the determination of strain components, Tectonophysics 803 (2021) 228754, https://doi.org/10.1016/j.tecto.2021.228754.
[25] X. Zhou, Z. Liu, B.-X. Xu, Influence of dislocations on domain walls in perovskite ferroelectrics: phase-field simulation and driving force calculation, Int. J. Solids Struct. 238 (2022) 111391, https://doi.org/10.1016/j.ijsolstr.2021.111391.
[26] C. Reimuth, B. Lin, Y. Yang, P. Stein, X. Zhou, B.-X. Xu, Chemo-mechanical study of dislocation mediated ion diffusion in lithium-ion battery materials, J. Appl. Phys. 130 (3) (Jul. 2021) 35103, https://doi.org/10.1063/5.0049502.
[27] C. V Di Leo, E. Rejovitzky, L. Anand, Diffusion–deformation theory for amorphous silicon anodes: the role of plastic deformation on electrochemical performance, Int. J. Solids Struct. 67–68 (2015) 283–296, https://doi.org/10.1016/j.ijsolstr.2015.04.028.
[28] P. Stein, Y. Zhao, B.-X. Xu, Effects of surface tension and electrochemical reactions in Li-ion battery electrode nanoparticles, J. Power Sources 332 (2016) 154–169, https://doi.org/10.1016/j.jpowsour.2016.09.085.
[29] H. Gomez, T.J.R. Hughes, Provably unconditionally stable, second-order time-accurate, mixed variational methods for phase-field models, J. Comput. Phys. 230 (13) (2011) 5310–5327, https://doi.org/10.1016/j.jcp.2011.03.033.
[30] A. Asheri, S. Rezaei, V. Glavas, B.X. Xu, Microstructure impact on chemo-mechanical fracture of polycrystalline lithium-ion battery cathode materials, Eng. Fract. Mech. 309 (July) (2024) 110370, https://doi.org/10.1016/j.engfracmech.2024.110370.
[31] Z.D. Hood, M. Chi, Mechanistic understanding and strategies to design interfaces of solid electrolytes: insights gained from transmission electron microscopy, J. Mater. Sci. 54 (15) (2019) 10571–10594, https://doi.org/10.1007/s10853-019-03633-2.
[32] P. Barai, A.T. Ngo, B. Narayanan, K. Higa, L.A. Curtiss, V. Srinivasan, The role of local inhomogeneities on dendrite growth in LLZO-based solid electrolytes, J. Electrochem. Soc. 167 (10) (2020) 100537, https://doi.org/10.1149/1945-7111/ab9b08.
[33] L. Yang, et al., Interrelated interfacial issues between a Li7La3Zr2O12-based garnet electrolyte and Li anode in the solid-state lithium battery: a review, J. Mater. Chem. A 9 (10) (2021) 5952–5979, https://doi.org/10.1039/D0TA08179E.
[34] R. Chen, et al., The thermal stability of lithium solid electrolytes with metallic lithium, Joule 4 (4) (2020) 812–821, https://doi.org/10.1016/j.joule.2020.03.012.
[35] X. Zhou, C. Reimuth, P. Stein, B.-X. Xu, Driving forces on dislocations: finite element analysis in the context of the non-singular dislocation theory, Arch. Appl. Mech. 91 (11) (2021) 4499–4516, https://doi.org/10.1007/s00419-021-02017-w.
[36] V. Voegelé, P. Cordier, V. Sautter, T.G. Sharp, J.M. Lardeaux, F.O. Marques, Plastic deformation of silicate garnets: II. Deformation microstructures in natural samples, Phys. Earth Planet. Inter. 108 (4) (1998) 319–338, https://doi.org/10.1016/S0031-9201(98)00111-3.
[37] V. Voegelé, J.I. Ando, P. Cordier, R.C. Liebermann, Plastic deformation of silicate garnets: I. High-pressure experiments, Phys. Earth Planet. Inter. 108 (4) (1998) 305–318, https://doi.org/10.1016/S0031-9201(98)00110-1.
[38] D.J.H. Cockayne, The principles and practice of the weak-beam method of electron microscopy, J. Microsc. 98 (2) (Jul. 1973) 116–134, https://doi.org/10.1111/j.1365-2818.1973.tb03815.x.
[39] R. Madec, B. Devincre, L. Kubin, T. Hoc, D. Rodney, The role of collinear interaction in dislocation-induced hardening, Science 301 (5641) (Sep. 2003) 1879–1882, https://doi.org/10.1126/science.1085477.
[40] D.O. Shin, et al., Synergistic multi-doping effects on the Li7La3Zr2O12 solid electrolyte for fast lithium ion conduction, Sci. Rep. 5 (1) (2015) 18053, https://doi.org/10.1038/srep18053.
[41] F.R.N. Nabarro, The theory of solution hardening, Philos. Mag. A J. Theor. Exp. Appl. Phys. 35 (3) (Mar. 1977) 613–622, https://doi.org/10.1080/14786437708235994.
[42] P. Li, Y. Zhao, Y. Shen, S.-H. Bo, Fracture behavior in battery materials, JPhys Energy 2 (2) (2020) 22002, https://doi.org/10.1088/2515-7655/ab83e1.